ROYAL SOCIETY OF CHEMISTRY

EDGE ARTICLE

Check for updates

Pre-synthetic redox control of structure and properties in copper TTFtt coordination polymers

Ningxin Jiang,[a] Saranya Velliyarat,[b] Chen-Yu Lien,[a] Ha L. Nguyen, [ID][a] Jan Hofmann, [ID][c] Jie-Hao Chen, [ID][d] Arun Ramanathan, [ID][e] Alexander S. Filatov, [ID][a] Henry S. La Pierre, [ID][e] Shrayesh Patel, [ID][d] Karena W. Chapman,[c] Jan-Niklas Boyn [ID][b] and John S. Anderson [ID]*[a]

Conductive coordination polymers (CPs) with sulfur-based ligands offer strong metal–ligand interactions and redox tunability, making them promising candidates for electronic applications. Tetrathiafulvalene-2,3,6,7-tetrathiolate (TTFtt) is a particularly attractive ligand. However, its strong metal–ligand covalency leads to rapid irreversible metal coordination, limiting control over structure and morphology. Here, we demonstrate structural control in Cu TTFtt CPs using a pre-synthetic redox control strategy. Two new copper-based CPs, **CuTTFtt** and **Cu₂TTFtt**, have been synthesized and thoroughly characterized from differentially oxidized TTFtt synthons. **CuTTFtt** forms a 1D chain, while **Cu₂TTFtt** adopts a 2D ribbon-like structure. Detailed spectroscopic studies confirm the structures of these materials as well as their ligand and metal oxidation states. Physical property measurements reveal that **Cu₂TTFtt** exhibits higher conductivity than **CuTTFtt**. Furthermore, **Cu₂TTFtt** also shows unusual diamagnetism which contrasts the paramagnetism observed in **CuTTFtt** and the related material **NiTTFtt**. Density functional theory (DFT) further elucidates the physical properties of these CPs and supports the observed conductivity trends. This study expands the structural landscape of TTFtt-based CPs and further establishes how redox-doping can tune CP structure and physical properties.

Introduction

Conductive coordination polymers (CPs) are a promising class of materials for electronic and optoelectronic applications, including in sensing, energy storage, and electrocatalysis.[1–12] Sulfur-based ligands are particularly attractive for constructing these materials due to their strong covalent bonding with transition metals, enabled by energetic matching and hence covalency between metals and sulfur.[13–19] Many sulfur-containing ligands are also redox-active, which allows for further tuning of chemical and physical properties.[20–23]

Of many possible sulfur-rich ligands, tetrathiafulvalene-2,3,6,7-tetrathiolate (TTFtt), which combines a tetrathiafulvalene (TTF) core—a well-known motif in conductive molecules—with dithiolene coordination sites, is an excellent candidate for designing highly conductive materials.[23–25] Several

reports have investigated the combination of this linker with transition metals, but it typically exhibits rapid reaction with metal cations. This rapid irreversible reaction makes it difficult to control CP structure or morphology, and syntheses with TTFtt often yield amorphous black powders which can be difficult to characterize despite being highly conductive.[26–29] Early synthetic efforts to generate TTFtt based CPs with both Ni and Cu resulted in conductive solids, but minimal insight into their electronic and geometric structure was obtained.[30] This lack of insight is largely due to challenging structural characterization which can be particularly difficult with thiolate-based systems.[31–34] Hoffmann and coworkers proposed several structures for TTFtt-based materials 40 years ago this year,[35] but only a 1D chain structure of **NiTTFtt** has been experimentally demonstrated.[23] Predictions of an alternative 2D sheet structure remain experimentally unverified.[36]

This dearth of detail presents a significant challenge in understanding (and controlling) the structure and properties of these materials. Dimensionality (1D, 2D, and 3D) plays a critical role over physical properties including both conductivity and magnetism, as demonstrated in both carbon-based materials and reticular structures.[37–39] However, studies on the dimensionality of sulfur-based frameworks are rare. This difficulty in building structure–function relationships is made even more challenging as sulfur-based ligands often feature multiple

[a] Department of Chemistry, University of Chicago, Chicago, Illinois, 60637, USA. E-mail: jsanderson@uchicago.edu

[b] Department of Chemistry, University of Minnesota, Minneapolis, Minnesota, 55455, USA

[c] Department of Chemistry, Stony Brook University, Stony Brook, New York, 11794, USA

[d] Pritzker School of Molecular Engineering, University of Chicago, Chicago, Illinois, 60637, USA

[e] School of Chemistry and Biochemistry, Georgia Institute of Technology, Atlanta, Georgia, 30332-0400, USA

accessible oxidation states which may change concurrently with changes in dimensionality.[20,21,40] Many CP syntheses occur in aerobic conditions which can lead to *in situ* oxidation.[41–43] This redox ambiguity complicates the determination of metal oxidation states, especially with redox-active metals such as Cu, where ambiguities in oxidation states are common in thiolate-based systems.[44,45] The redox activity of ligands combined with the structural challenges mentioned above, make understanding and controlling the properties of TTFtt-based materials particularly challenging.

We recently employed a transmetalation and pre-synthetic doping strategy to successfully synthesize Ni CPs of TTFtt with variable TTFtt oxidation states.[40,46] Using a pre-oxidized TTFtt transmetalating synthon provides **NiTTFtt** with a 1D chain structure where TTFtt is in a formally doubly oxidized state. While **NiTTFtt** displays high conductivity despite an amorphous structure, its reduced congener **Li-NiTTFtt**, with an overall TTFtt^{4-} ligand, displays intriguing photothermoelectric and thermoelectric properties.

This progress in understanding the structure and electronic properties of **NiTTFtt** motivates extending this synthetic control to other transition metal centers. Copper-thiolate CPs are known to exhibit electrical conductivity comparable to that of nickel-thiolate materials.[45,47,48] We have therefore investigated copper coordination chemistry with TTFtt and synthesized two new materials, **CuTTFtt** and **Cu$_2$TTFtt**. By employing similar pre-synthetic redox control of transmetalating TTFtt reagents, we can manipulate TTFtt oxidation states, with **Cu$_2$TTFtt** containing TTFtt^{3-} linkers and **CuTTFtt** containing oxidized TTFtt^{2-} linkers. Thorough characterization, including X-ray absorption spectroscopy (XAS), X-ray photoelectron spectroscopy (XPS), and Raman spectroscopy, enable an accurate determination of ligand and copper oxidation states.

Structural analyses suggest that while **CuTTFtt** adopts a 1D chain structure similar to **NiTTFtt**, while **Cu$_2$TTFtt** forms a 2D ribbon-like layered structure consistent with original structural models proposed by Hoffman and coworkers.[35] Conductivity measurements demonstrate that **Cu$_2$TTFtt** shows higher conductivity compared to **CuTTFtt**. In contrast to the dominant Pauli paramagnetism observed in **NiTTFtt**, **Cu$_2$TTFtt** also shows diamagnetic behavior while **CuTTFtt** exhibits Curie–Weiss paramagnetism. Density functional theory (DFT) calculations were also employed to provide insight into the different physical properties of **NiTTFtt**, **CuTTFtt**, and **Cu$_2$TTFtt** and validate the observed experimental trends.

These findings validate and expand the known structural types for TTFtt-based CPs and also elucidate how these structures influence charge transport properties. Moreover, the different morphologies observed for these copper-based CPs suggest that linker redox-tuning is an important strategy for controlling structure. This study motivates continued investigations into how the structure and metal identity of TTFtt-based materials dictates magnetic coupling and novel emergent properties at the interface of conductivity and magnetism.

Results and discussion

Synthesis of CuTTFtt and Cu$_2$TTFtt

The syntheses of **CuTTFtt** and **Cu$_2$TTFtt** utilize transmetalation with TTFtt(SnBu$_2$)$_2{}^{n+}$ reagents (n = 0 or 2) due to the ability to program a desired TTFtt redox state prior to CP synthesis (Fig. 1).[22] **CuTTFtt** was synthesized following a similar procedure to **NiTTFtt**.[23] First, TTFtt(SnBu$_2$)$_2$ was oxidized using Fc^{Bzo}BAr$_4^F$ (Fc^{Bzo} = benzoylferrocenium and BAr$_4^F$ = tetrakis[3,5-bis(trifluoromethyl)phenyl]borate) in dichloromethane (DCM). Separately, CuCl$_2$ was dissolved in methanol (MeOH) and
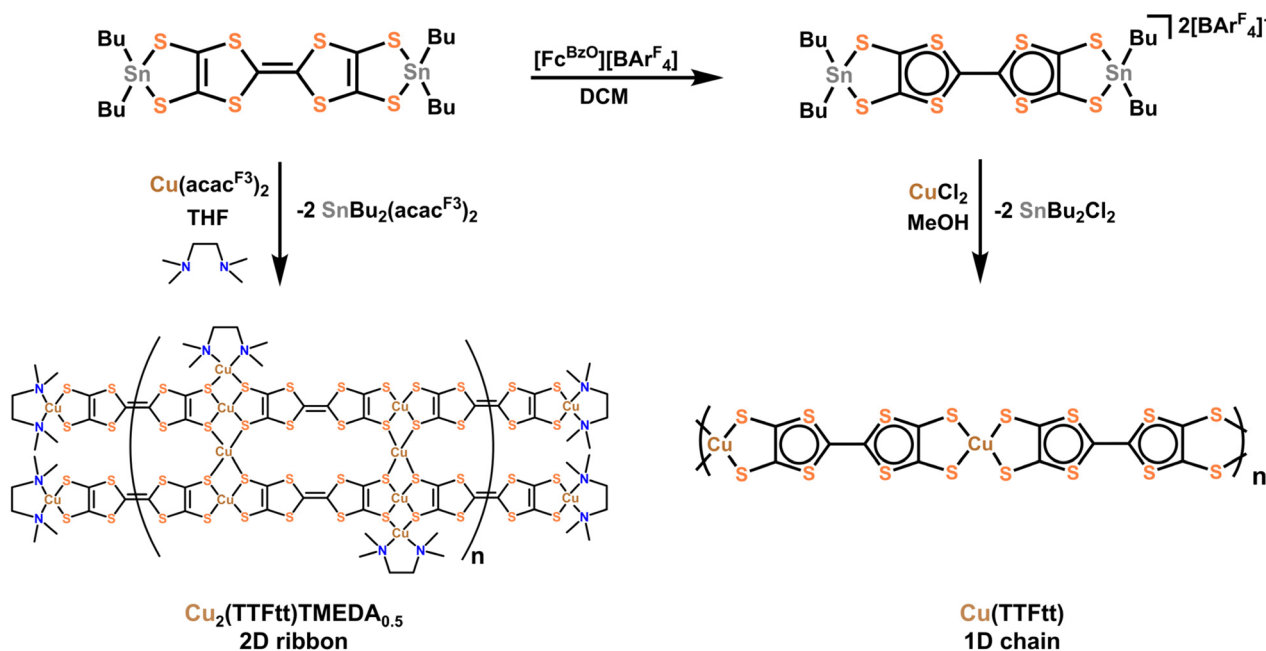

Fig. 1 Synthetic scheme for **Cu$_2$TTFtt** (left) and **CuTTFtt** (right).

subsequently mixed with a DCM solution of oxidized TTFtt(SnBu$_2$)$_2$. A black powder (**CuTTFtt**) quickly formed and was isolated after workup.

For **Cu$_2$TTFtt**, two equivalents of Cu(acac^{F3})$_2$ (acac^{F3} = trifluoroacetylacetonate) were mixed with excess tetramethylethylenediamine (TMEDA) in tetrahydrofuran (THF), then combined with one equivalent of TTFtt(SnBu$_2$)$_2$ in THF to immediately generate a dark powder. It is worth noting that the addition of TMEDA to a Cu(acac^{F3})$_2$ solution initially results in an immediate color change from blue to green, suggesting the formation of [(Cu(TMEDA)$_2$)]$^{2+}$. The isolated dark green (nearly black) powder was dried at 70 °C to yield **Cu$_2$TTFtt**.

Composition

X-ray fluorescence (XRF) analysis was initially used to determine the elemental composition of **Cu$_2$TTFtt** and **CuTTFtt** (SI, Fig. S1 and Table S1). The Cu : S ratio is 1 : 3.78 for **Cu$_2$TTFtt** and 1 : 9.7 for **CuTTFtt** corresponding to Cu : TTFtt ratios of ~2 : 1 and ~1 : 1, respectively. Minimal Sn content (<1% atomic ratio relative to Cu) was detected in both samples, indicating that copper effectively transmetalates tin in the TTFtt linkers. Combustion analysis for **CuTTFtt** reveals 19.99(8)% carbon, and 0.49(2)% hydrogen, suggesting negligible organic components beyond TTFtt. These results align with minimal mass loss observed below 200 °C in thermogravimetric analysis (TGA, Fig. S2). Based on this data, the chemical formula of **CuTTFtt** is most consistently assigned as CuC$_6$S$_8$ (Cu(TTFtt)).

For **Cu$_2$TTFtt**, combustion analysis yields 21.36(1)% carbon, 2.72(3)% nitrogen, and 1.75(3)% hydrogen. These results suggest some additional organic component beyond a limiting formula of Cu$_2$C$_6$S$_8$. Combined with a ~10% mass loss observed at ~200 °C in TGA (Fig. S2), we propose a chemical formula for **Cu$_2$TTFtt** as Cu$_2$C$_6$S$_8$(C$_6$H$_{16}$N$_2$)$_{0.5}$ (Cu$_2$(TTFtt)(TMEDA)$_{0.5}$) with the inclusion of 0.5 TMEDA molecules per formula unit. The inclusion of TMEDA suggests a fundamentally different structure for **Cu$_2$TTFtt**. The proposed chemical formulas of both **CuTTFtt** and **Cu$_2$TTFtt** match well with the combustion analysis results shown in Table S2.

Structural analysis

Both lab-based (Cu source, $\lambda = 1.541$ Å) and synchrotron ($\lambda = 0.167$ Å) sources were used for powder X-ray diffraction (PXRD) measurements to elucidate the structures of **CuTTFtt** and **Cu$_2$TTFtt**. Lab-based PXRD analysis of **CuTTFtt** reveals no sharp Bragg peaks with only a very broad feature between about 23 and 30° 2θ that is indicative of a structure with low crystallinity (Fig. S3A). In contrast, **Cu$_2$TTFtt** reveals two broad peaks centered at about 7.6° and 25.6°, suggesting a somewhat higher degree of crystallinity compared to **CuTTFtt** and most reported TTFtt-based CPs. The synchrotron PXRD patterns reveal substantially more diffraction peaks (Fig. 2A). The presence of TMEDA was found to be essential for obtaining crystalline samples (Fig. S3B). The PXRD pattern and carbon content of **Cu$_2$TTFtt** remain unchanged after heating at 160 °C for 6 hours
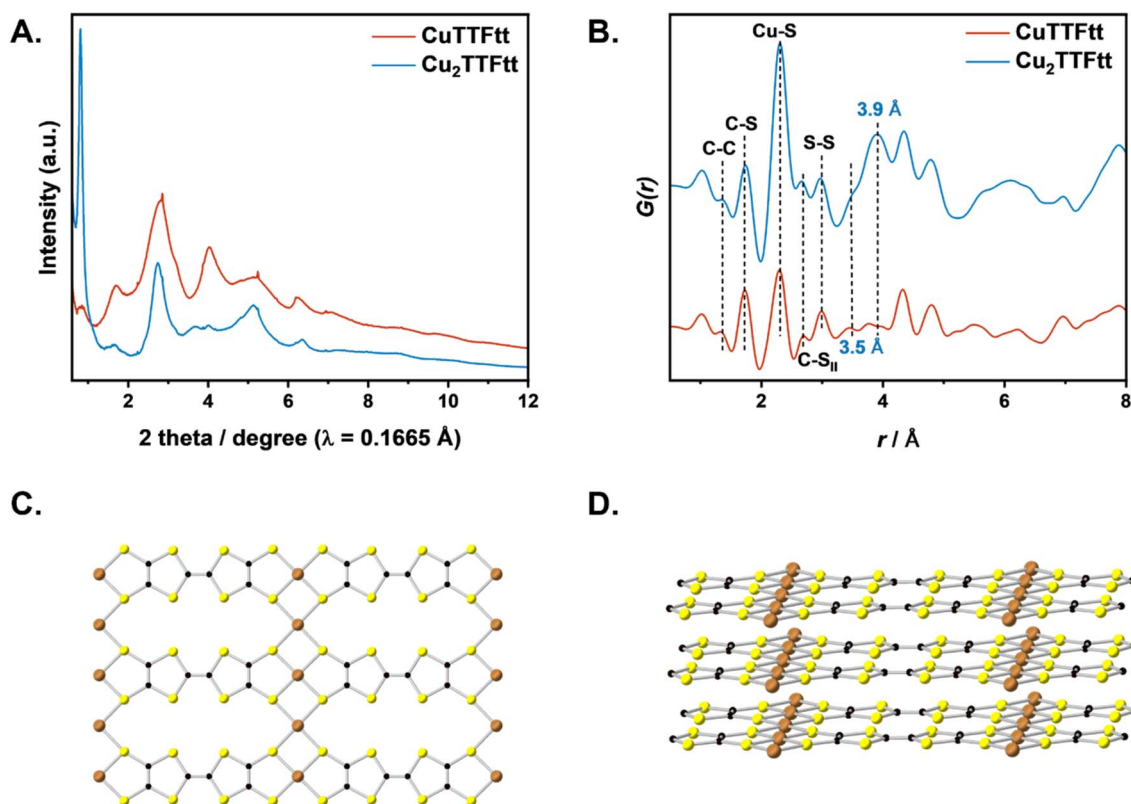

Fig. 2 (A) Synchrotron ($\lambda = 0.167$ Å) PXRD patterns and of **Cu$_2$TTFtt** and **CuTTFtt**, (B) PDF of **Cu$_2$TTFtt** and **CuTTFtt**. Structural model of **Cu$_2$TTFtt** viewed along c-axis (C) and viewed from a-axis (D).

despite the boiling point of TMEDA being approximately 120 °C. This suggests that TMEDA strongly binds to the framework, playing a critical structural role in **Cu₂TTFtt**.

Pair distribution function (PDF) data (Fig. 2C and S5A) reveal local range order in these CPs. The low r region of the PDF data for both materials contains features at ~1.4 Å, 1.8 Å, 2.3 Å, 2.7 Å and 3.0 Å that correspond to the C–C, C–S, Cu–S, C⋯S, and S⋯S distances, respectively (Fig. 2D and S5). These peaks correspond to intra-chain atomic distances within **CuTTFtt** and **Cu₂TTFtt** and thus verify the presence of 1D chains in both materials. The PDF of **CuTTFtt** can be well-described by a single-chain model derived from **NiTTFtt** (Fig. S6). The difference in peak position between model and data around 2.3 Å is due to different Cu–S bond lengths compared with Ni–S distances from the **NiTTFtt** model.[23]

The PDF of **Cu₂TTFtt** shows distinct differences in local order from the 1D materials, particularly in the intensity of the Cu–S peak at 2.3 Å and the presence of additional peaks at 3.5 Å and 3.9 Å. A similar 3.9 Å distance has been associated with a side-by-side ligand arrangement in other TTF based materials,[49] and so the presence of this feature in **Cu₂TTFtt** suggests the presence of such a side-by-side TTFtt arrangement. Combined with the increased Cu–S intensity observed in the PDF of **Cu₂TTFtt**, we propose that these increased peak intensities correspond to additional Cu^{2+} ions that bind to sulfur in between negatively charged $CuTTFtt^{2-}$ chains in a side-by-side arrangement (Fig. 2C, D and 3). As previously mentioned, a structural model for tetrathiolate-based materials with a metal-to-ligand ratio of 2 : 1 was previously proposed by Hoffmann and coworkers in 1985, but experimental validations have been lacking until the present example for **Cu₂TTFtt**. This model has also been proposed as a potential structure for [Cu_x(Cu-ETT)] systems.[35,36] We therefore propose a related 2D model for **Cu₂TTFtt** with additional Cu–S bonds, which is consistent with the larger peak at 2.3 Å in the PDF data (Fig. S5B). This model consists of a 2D layered framework where copper cations connect 1D chains (Fig. 2C, D and S7). Consistent with prior data on TTFtt materials, the interlayer distance is 3.62 Å and the distance between neighboring Cu centers is 12.6 Å within a Cu–TTFtt chain. It should be noted that this construct is an idealized highly symmetric model of the material and requires a perfect 1D chain length match and alignment when propagating along the second dimension. Any mismatch in these distances/alignments would lead to disorder in the material and formation of amorphous to semi-crystalline materials as observed experimentally.

The simulation of the PXRD pattern based on this idealized model using *Pmmm* space group and a unit cell of $a = 6.67$ Å, $b = 12.61$ Å, $c = 3.62$ Å ($V = 304.3$ Å³) reasonably reproduces the general features of the experimental diffraction pattern. This motivated the use of this model for a crude Rietveld refinement. This analysis is admittedly limited due to the poor crystallinity of **Cu₂TTFtt**, but the Rietveld refinement does show a reasonable fit with the experimental data which provides some validation of the proposed structural model (Fig. S9). The refined unit cell parameters are $a = 6.613(11)$ Å, $b = 12.991(8)$ Å, $c = 3.6136(20)$ Å ($V = 310.4(6)$ Å³) with R and wR factors of 0.042 and 0.051 respectively. The only sharp Bragg peak is located at $Q =$
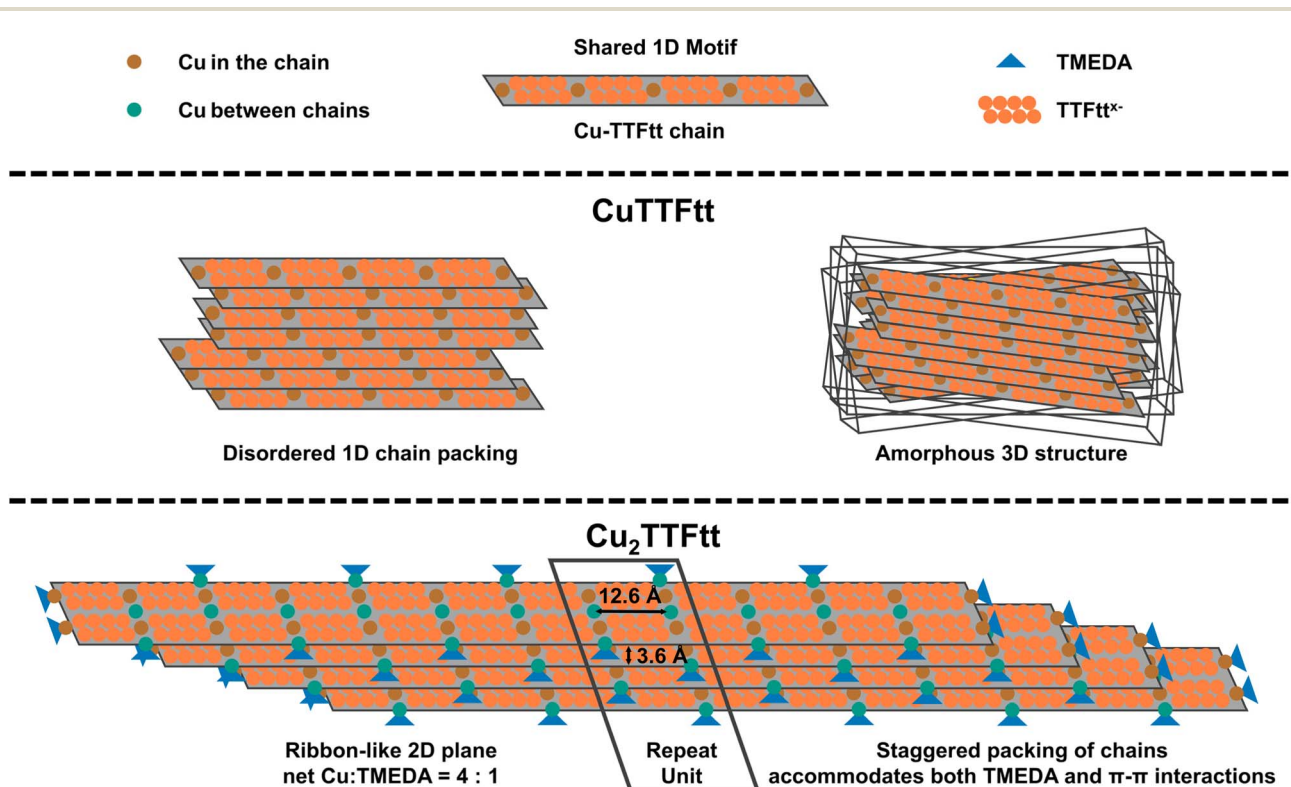

Fig. 3 Demonstration of proposed structural models of **CuTTFtt** (middle) and **Cu₂TTFtt** (bottom) based on PXRD, PDF and elemental analysis.

0.53 Å^{-1} and is assigned to a (010) reflection suggesting a more precise long-order arrangement of 1D chains in the structure compared to all other dimensions. The crystallite size (as refined over the whole powder pattern) is ~7 nm, which is indicative of 5 to 6 Cu–TTFtt motifs in a single chain or ~20 Cu$_2$TTFtt layers. While this domain size is reasonable for a material with defects and disorder, it should be emphasized that this value is highly sensitive to both the sample's low crystallinity and to the limitations of our structural model. As such, the reported crystallite size should be regarded as an approximate lower bound rather than an absolute measurement.

While these X-ray analyses provide a reasonable structure for **Cu$_2$TTFtt**, composition studies reveal a significant amount of TMEDA which is unaccounted for in the structural model. Attempts to incorporate TMEDA into the 2D plane or between the 2D planes do not produce physically reasonable models due to steric clashes. We instead propose that TMEDA binds exclusively to copper at the edge sites of **Cu$_2$TTFtt**. TMEDA is known to act as a bidentate ligand for copper, forming complexes such as [Cu(TMEDA)L$_x$] or [Cu(TMEDA)$_2$]$^{1+/2+}$. When L represents sulfur-based ligands, a square planar geometry is reasonably expected in [Cu(TMEDA)L$_2$].[50] Given that Cu cations bind strongly to sulfur-based ligands, we propose that Cu(TMEDA)$^{1+/2+}$ resides at the terminal positions of each Cu–TTFtt chain in **Cu$_2$TTFtt**. A structural model was generated to allow AA stacking of Cu–TTFtt chains with TMEDA termination, as shown in Fig. S10. After structural optimization, the interlayer distance increased to 6.5 Å, which is longer than the expected 3.6 Å from PXRD data and suggests that Cu(TMEDA) complexes cannot stack directly on top of each other from different chains (Fig. S10). However, a structural model with TMEDA present only at terminal positions cannot account for the Cu : TMEDA ratio of 4 unless each chain consists of only four TTFtt anions, which is inconsistent with the strong (010) peak observed at 0.80° 2θ (l = 0.167 Å). The experimentally observed Cu : TMEDA ratio can only be achieved if two Cu–TTFtt chains are coupled in **Cu$_2$TTFtt**, as illustrated in Fig. 3 and S12. The resulting structural model, shown in Fig. 3, demonstrates a chemical formula of Cu$_2$TTFtt(TMEDA)$_{0.5}$, which aligns well with the compositional analysis and avoids TMEDA steric clashes. Thus, the combined experimental data support that **Cu$_2$TTFtt** adopts a 2D ribbon-like layered structure similar to that shown in Fig. 3.

We note that, despite the stoichiometric amount of TMEDA present, no distinct peak corresponding to TMEDA can be identified in the PDF analysis of **Cu$_2$TTFtt** (Fig. 2B). This absence can be attributed to two factors. Firstly, reasonable Cu–N bond lengths (~1.9 Å) have significant overlap with the numerous C–S bonds in the material. Secondly, the number of proposed Cu–N bonds is much smaller than the other bonds represented in the PDF analysis, resulting in a lower signal intensity that cannot be directly observed.

To further characterize the structures of **Cu$_2$TTFtt** and **CuTTFtt**, we carried out Cu K-edge XAS measurements and analyzed the EXAFS data (Fig. S13, S14, Tables S3 and S4). For **CuTTFtt**, the best-fit results yield a Cu–S distance of 2.28 Å,

a Cu–C distance of 3.13 Å, and an average Cu coordination number of 4.0 ± 0.2. These values are consistent with previously reported Cu–S bond lengths and with our PDF analysis,[51] confirming that Cu in **CuTTFtt** adopts a square-planar coordination environment. This finding further supports the conclusion that the structure of **CuTTFtt** closely resembles that of **NiTTFtt**, forming a one-dimensional chain-like arrangement.

For **Cu$_2$TTFtt**, the EXAFS fitting gives a Cu–N distance of 1.76 Å, a Cu–S distance of 2.27 Å, a Cu–Cu distance of 2.95 Å, and a Cu–C distance of 3.14 Å, with an average Cu coordination number of 4.1 ± 0.4. The Cu–S bond length again agrees well with the PDF analysis, confirming that Cu also adopts a square-planar geometry in this compound. The relative ratio of Cu–N to Cu–S bonds (1 : 8) is close to the theoretical value of 1 : 7, consistent with the presence of stoichiometric TMEDA in the structure. Together, these EXAFS results provide direct structural support that **Cu$_2$TTFtt** adopts a two-dimensional ribbon-like framework.

Ligand redox state analysis

One advantage of using TTFtt(SnBu$_2$)$_2$$^{n+}$ transmetalating agents is the well-defined TTF oxidation state which should translate into the resulting CP. However, *in situ* redox chemistry can frequently occur, and so rigorous characterization is necessary to confirm the proposed oxidation states of the TTFtt linker and Cu centers in the obtained materials. Normally, such an analysis would begin with characterization of the Cu oxidation states. However, the oxidation states of Cu centers can be notoriously difficult to concretely assign, particularly in covalent sulfur-based materials. Indeed, both XPS and XAS data provide somewhat ambiguous results (see SI Section 4).[44,45,52,53]

Recent sulfur K-edge XAS studies on Ni-TTFtt molecules indicate that the first pre-edge feature in doubly oxidized TTFtt^{2-} appears ~0.6 eV lower in energy than the pre-edge feature in both neutral TTFtt^{4-} and singly oxidized TTFtt^{3-}.[54] This provides a useful benchmark to examine the oxidation state of TTFtt linkers in these copper-based materials. We therefore collected sulfur K-edge XAS data on both **Cu$_2$TTFtt** and **CuTTFtt** (Fig. 4A). Molecular analogs of copper TTFtt compounds have not yet been successfully synthesized, so we compared the observed spectroscopic features to those of analogous nickel compounds for interpretation. For **CuTTFtt**, the first pre-edge feature is observed at 2470.4 eV, while in **Cu$_2$TTFtt**, a shoulder-like feature appears at approximately 2471.2 eV. The 0.8 eV energy difference between the two samples strongly suggests that the TTFtt motifs are in different overall redox states. By comparison, the sulfur K-edge pre-edge feature for **NiTTFtt** appears at 2470.7 eV, supporting that the linkers in **CuTTFtt** are best assigned with a formal oxidation state of TTFtt^{2-}. However, the pre-edge positions for TTFtt^{3-} and TTFtt^{4-} are similar, and so the redox state of TTFtt in **Cu$_2$TTFtt** cannot be determined from sulfur K-edge XAS data alone.

To further investigate the formal TTFtt redox state, Raman spectroscopy and XPS were employed. Infrared signals were difficult to interpret due to broadening, presumably from high
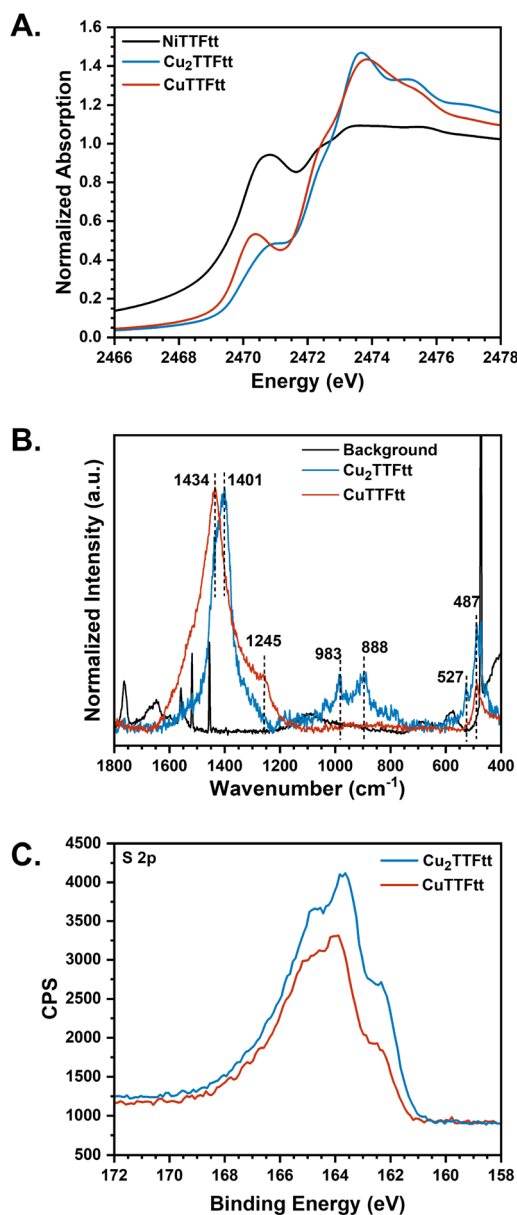
Fig. 4 Spectroscopic studies TTFtt ligand redox states. (A) Sulfur K-edge XAS, (B) Raman spectra, and (C) S 2p XPS spectra of **Cu$_2$TTFtt** and **CuTTFtt**.

reflectivity/shielding from potential metallic character (Fig. S15). The Raman spectra for **Cu$_2$TTFtt** and **CuTTFtt** are more informative and are shown in Fig. 4B. Both compounds show peaks between 1400-1450 cm^{-1} which can be assigned to C–C vibrations.[55] For **Cu$_2$TTFtt**, this feature is centered at 1401 cm^{-1}, compared to 1434 cm^{-1} in **CuTTFtt**. This shift to a lower wavenumber in **Cu$_2$TTFtt** suggests differences in C–C bonding order, likely indicating longer C–C bond lengths in **Cu$_2$TTFtt** and thus a more reduced formal oxidation state of the TTFtt linkers. Similar trends have been observed in **NiTTFtt** coordination complexes, where oxidation of the TTFtt motif decreases C–C bond length.[40] In CPs such as **NiTTFtt** (TTFtt^{2-}) and **Li-NiTTFtt** (TTFtt^{4-}), oxidized TTFtt CPs consistently show C–C vibrations at higher wavenumbers.[23,40] Thus, the higher

frequency features observed in **CuTTFtt** *vs.* **Cu$_2$TTFtt** further support more reduced TTFtt linkers in **Cu$_2$TTFtt**.

Additional peaks are present around 900 cm^{-1} which can be assigned to C–S vibrations. These features are present in **Cu$_2$-TTFtt** and **Li-NiTTFtt** but are absent in **CuTTFtt**,[55] and so we hypothesize that they may serve as a characteristic Raman signal for reduced TTFtt linkers (*i.e.* TTFtt^{4-}).[40] Overall, the observed Raman features strongly support the assignment of TTFtt in **Cu$_2$TTFtt** as having a lower redox state than in **CuTTFtt**. Both samples also show a peak at 487 cm^{-1} which arises from Cu–S vibrations. However, **Cu$_2$TTFtt** shows an extra peak at 527 cm^{-1} which indicates an additional sulfur ligation environment in **Cu$_2$TTFtt** and further supports the proposed 2D ribbon structure.

Sulfur 2p XPS data was finally collected to further corroborate the TTFtt oxidation states (Fig. 4C). Notably, both **Cu$_2$TTFtt** and **CuTTFtt** exhibit a main peak accompanied by two shoulder-like features. Deconvolution of the spectra into three distinct sulfur chemical states yields a reasonable fit, as shown in Fig. S17. Based on previous XPS analyses of poly[Cu$_x$(Cu-ETT)],[36] the first two sets of doublets can be assigned to the reduced terminal sulfur (162.5 eV) and the oxidized terminal sulfur (164.1 eV) in the TTFtt ligand. The broad doublets at higher binding energy (164.8 eV) correspond to sulfur within the TTF core. Notably, the ratio of oxidized sulfur to reduced sulfur, determined from peak areas, increases from 1.20 in **Cu$_2$TTFtt** to 2.15 in **CuTTFtt**, confirming a more oxidized redox state of TTFtt in **CuTTFtt**. Interestingly, the 162 eV feature, which intensifies with increasing oxidation of TTFtt, has also been observed in **NiTTFtt** (Fig. S18), poly[Cu$_x$(Cu-ETT)], and Li$_x$Fe$_3$(-THT)$_2$.[21,23,36] This observation highlights XPS as a powerful tool for studying ligand redox states.

Finally, we examined the Cu K-edge XANES spectra of **CuTTFtt** and **Cu$_2$TTFtt** (Fig. S20). The absorption edge of **Cu$_2$-TTFtt** is clearly shifted to lower energy relative to that of **CuTTFtt**. Since the Cu K-edge position decreases with decreasing oxidation state, this shift indicates the presence of a more reduced copper component in **Cu$_2$TTFtt**. Together with the spectroscopic evidence for TTFtt^{2-} ligands in **CuTTFtt**, this strongly supports a Cu^{2+} assignment in this compound, giving an overall formal redox state of (Cu^{2+})(TTFtt^{2-}). For **Cu$_2$TTFtt**, the ligand is expected to be either TTFtt^{3-} or TTFtt^{4-}; considering the lower edge position and the presence of a more reduced copper species, the most reasonable assignment is a mixed-valent state of (Cu^{2+})(Cu^{+})(TTFtt^{3-}).[51]

Physical property studies

The electrical and magnetic properties of **Cu$_2$TTFtt** and **CuTTFtt** were then analyzed (Fig. 5). A room-temperature four-point electrical conductivity of 50(2) S cm^{-1} for **Cu$_2$TTFtt** and 23(2) S cm^{-1} for **CuTTFtt** were obtained. These values are high among those reported for most conductive CPs. Comparison of these values to those for **NiTTFtt** materials is informative. The reduced compound **Li-NiTTFtt**, which has TTFtt in a reduced state similar to **Cu$_2$TTFtt**, shows a considerably lower conductivity (10(1) S cm^{-1}), while **NiTTFtt** with oxidized TTFtt linkers is
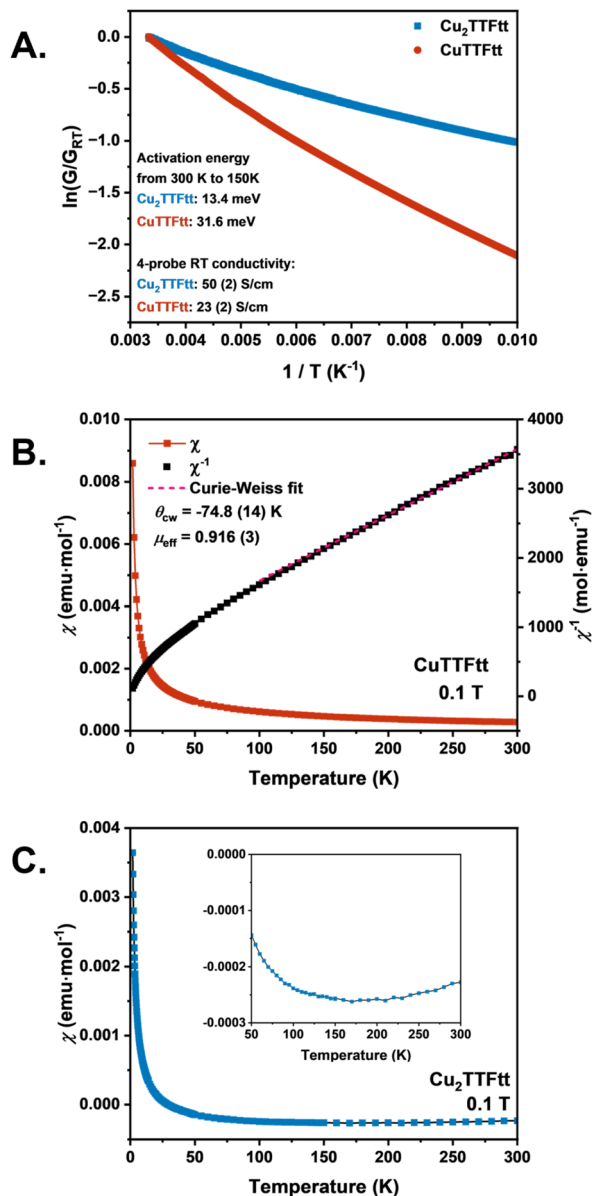
Fig. 5 Charge transport and magnetic properties of **CuTTFtt** and **Cu₂TTFtt**. (A) Variable temperature resistance measurements. (B) Variable temperature magnetic susceptibility measurements of **CuTTFtt** at 0.1*T*. Curie–Weiss fit in pink. (C) Variable temperature magnetic susceptibility measurements of **Cu₂TTFtt** at 0.1*T*. Inset shows negative susceptibility, supporting diamagnetism.

dramatically more conductive $(4.7(3) \times 10^2 \text{ S cm}^{-1})$.[23,40] Since **Li-NiTTFtt** adopts a 1D chain structure, the higher conductivity of **Cu₂TTFtt** compared to both **Li-NiTTFtt** and **CuTTFtt** suggests that the 2D ribbon-like structure enhances charge transport.

Additional data were then collected to further understand the charge transport properties of **CuTTFtt** and **Cu₂TTFtt**. Both materials show increased resistance with decreasing temperature (Fig. 5A). Fitting the temperature-dependent conductivity data from 300 K to 150 K yields activation energies of 13.4 meV for **Cu₂TTFtt** and 31.6 meV for **CuTTFtt**. The smaller activation energy in **Cu₂TTFtt** suggests either a higher carrier density or

mobility in **Cu₂TTFtt** than in **CuTTFtt**. The UV-vis-NIR spectra (Fig. S21) show no sharp absorbance drop for either compound, indicating a band gap smaller than 0.62 eV, consistent with the small activation energy values. Ultraviolet photoelectron spectroscopy (UPS) allows for the determination of work functions of 4.27 eV for **Cu₂TTFtt** and 4.47 eV for **CuTTFtt** (Fig. S22). Notably, for both compounds, the counts per second (CPS) drop to background levels at 0 eV, indicating a low or zero density of states at the Fermi level. The valence band maxima were determined to be 0.23 eV for **Cu₂TTFtt** and 0.63 eV for **CuTTFtt**. These results suggest that both compounds are small-bandgap semiconductors, differing from the glassy metallic behavior observed in **NiTTFtt**. This is also consistent with the lower electrical conductivity values observed for both compounds compared to **NiTTFtt**. The Seebeck coefficients are 10.9(2) μV K^{-1} for **Cu₂TTFtt** and −2.5(5) μV K^{-1} for **CuTTFtt**. In comparison, **Li-NiTTFtt** exhibits a Seebeck coefficient of 10 μV K^{-1}, while **NiTTFtt** has a value of −3.6 μV K^{-1}. Notably, materials where TTFtt is in a more reduced state (**Cu₂TTFtt** and **Li-NiTTFtt**) exhibit p-type behavior, whereas those where TTFtt is in a more oxidized state (**CuTTFtt** and **NiTTFtt**) exhibit n-type behavior. This trend underscores the critical role of ligand redox states in tuning the electronic structure and determining the charge-carrier type in TTFtt-containing materials.

The magnetic properties of both **CuTTFtt** and **Cu₂TTFtt** were also investigated, as shown in Fig. 5B and C. In contrast to **NiTTFtt**, which contains square planar Ni^{2+} cations in a closed shell diamagnetic $3d^8$ electron configuration, both copper compounds presented here contain Cu^{2+} cations, which have a $3d^9$ electronic configuration and are $S = 1/2$, potentially leading to magnetic behavior. For **CuTTFtt** the temperature dependence of the magnetic susceptibility (χ) increases monotonically with decreasing temperature from 300 to 1.8 K, consistent with paramagnetic behavior (Fig. 5B). As **CuTTFtt** exhibits high electrical conductivity, a small band gap, and $S = 1/2$ spin centers, some combination of both Pauli and Curie–Weiss paramagnetism is reasonable.[56] Fitting the data from 150 K to 300 K using the Curie–Weiss law yields a Curie–Weiss temperature (θ_{CW}) of −74.8(14) K, Curie constant of 0.105 emu K mol^{-1} and an effective magnetic moment of $0.916(3)\mu_B/Cu^{2+}$, which is lower than the expected $1.73\mu_B/Cu^{2+}$ for $S = 1/2$ spins. The χT value at room temperature is 0.08 emu K mol^{-1} (Fig. S25C), which is also significantly lower than the expected spin-only value of 0.375 emu K mol^{-1}. The field dependence of magnetization at 1.8 K slowly increases nonlinearly to $0.037\mu_B/Cu^{2+}$ up to 7T (Fig. S25D).

To differentiate the contributions of Pauli and Curie–Weiss paramagnetism in TTFtt²⁻-based CPs, a modified Curie–Weiss law, $\chi = C/(T - \theta_{CW}) + \chi_0$, incorporating a temperature-independent component (χ_0), was used to fit the temperature dependence of the magnetic susceptibility for both **CuTTFtt** and **NiTTFtt** (Fig. S26) from 100 K to 300 K.[56] Diamagnetic corrections were applied prior to fitting, ensuring that χ_0 primarily represents the Pauli paramagnetic contribution. For **NiTTFtt**, $C = 0.0797$ emu K mol^{-1}, $\chi_0 = 3.28 \times 10^{-4}$ emu mol^{-1} and $\theta_{CW} = 3.6$ K, indicating paramagnetism dominated by Pauli contributions. In contrast, for **CuTTFtt**, $C = 0.0739$ emu K mol^{-1}, $\chi_0 = $

3.40×10^{-5} emu mol^{-1} and $\theta_{CW} = -45.8$ K, suggesting a stronger Curie–Weiss paramagnetic component due to the higher absolute θ_{CW} value and lower χ_0. A possible conclusion from this fit is a lower number of carriers in **CuTTFtt**, leading to a smaller Pauli contribution, alongside antiferromagnetic coupling between either copper- or TTFtt-based spins. The interplay of antiferromagnetic coupling with carrier density or mobility remains an interesting arc of investigation in these materials.

For **Cu₂TTFtt** (Fig. 5C), the magnetic susceptibility (χ) is negative and extremely small ($\sim 10^{-4}$ emu mol^{-1}) down to 30 K even after accounting for diamagnetic corrections. The χT value is also negative at room temperature (-0.07 emu K mol^{-1}, Fig. S25A). The magnetization at 1.8 K and 7T is only $0.01\mu_B$, indicating that **Cu₂TTFtt** exhibits diamagnetic behavior despite the presence of Cu^{2+} cations (Fig. S25B). The diamagnetic behavior of **Cu₂TTFtt** suggests significant antiferromagnetic coupling leading to a strongly insulated singlet ground state.

To further investigate the nature of the spin centers in both compounds, we carried out X-band EPR measurements at 4 K (Fig. S27). The data were fitted using the EasySpin software[57] with one and two $S = 1/2$ spin centers in **Cu₂TTFtt** and **CuTTFtt**, respectively (Table S5, see SI for details). For **Cu₂TTFtt**, only a single $S = 1/2$ resonance was observed at $g = 2.011$. This g-value and the observed sharp linewidth are characteristic of an organic radical and we therefore assign this signal to radical TTFtt^{3-} linkers. SQUID susceptibility measurements show that **Cu₂TTFtt** is diamagnetic between 100 and 300 K, but exhibits a Curie tail at low temperature, supporting a small amount of magnetic impurities. Taken together, these results suggest strong antiferromagnetic exchange between Cu^{2+} and TTFtt^{3-} in **Cu₂TTFtt**, which suppresses the Cu^{2+} EPR signal while leaving a small but detectable fraction of unpaired TTFtt^{3-} spins, likely from defects or disorder. This finding also provides further support for a formal redox-state assignment of **Cu₂TTFtt** as (Cu^{2+})(Cu^{+})(TTFtt^{3-}).

In contrast, the EPR spectrum of **CuTTFtt** displays two distinct $S = 1/2$ resonances. A narrow and weak signal at $g = 2.005$ ($\sim 1\%$ of total intensity) can be attributed to trace radicals, likely from TTFtt^{3-} defects. The dominant broader resonance at $g = 2.036$ ($\sim 99\%$ of the signal intensity) can be reasonably assigned to uncoupled Cu^{2+} spin centers based on comparison with other Cu dithiolenes.[58] This assignment is also consistent with the SQUID susceptibility results, which indicate antiferromagnetic interactions between $S = 1/2$ Cu^{2+} ions.

Thus, the EPR results reveal that while **CuTTFtt** contains some Cu^{2+} spins with only a negligible amount of radical impurities, **Cu₂TTFtt** exhibits suppressed Cu^{2+} signals due to strong Cu^{2+}–TTFtt^{3-} antiferromagnetic interactions and some residual radical signatures from the TTFtt^{3-} linkers. These results provide additional confirmation of our proposed redox state assignments for both compounds.

Theoretical calculations

Density functional theory (DFT) calculations were performed to gain a deeper understanding of the electronic transport and magnetic behaviors of **CuTTFtt** and **Cu₂TTFtt** and to compare them with **NiTTFtt**. The Vienna Ab initio Simulation Package (VASP)[59–61] was used to perform first-principles calculations. The Perdew–Burke–Ernzerhof (PBE)[62] exchange correlation functional was used within the Generalized Gradient Approximation (GGA). The Projector Augmented-Wave (PAW)[63,64] method was used with the potentials PAW_PBE Cu for Cu, PAW_PBE C for C, PAW_PBE S for S and PAW_PBE Ni for Ni, respectively. The plane wave basis set was truncated at an energy cutoff of 800 eV for **CuTTFtt** and **Cu₂TTFtt**, and 700 eV for **NiTTFtt**, yielding convergence of the total energy to 1 meV per atom. The Brillouin zone was sampled using a gamma-point centered $5 \times 5 \times 5$ k-grid for all structural optimizations, a $7 \times 7 \times 7$ k-grid for density of states (DOS) calculations, and a k-path determined from SeeK-path[65–67] is used for band structure calculations. All calculations employed a SCF convergence criterion for the total energy of 10^{-8} eV with a Gaussian smearing width of 0.05 eV. For ionic relaxations, a force convergence criterion of 5 meV Å^{-1} was applied. van der Waals interactions were included via the DFT-D3 method with Becke–Johnson damping.[68] All the band structure and DOS plots were generated using Sumo.[69] The net atomic charge was calculated using Chargemol program by performing Density Derived Electrostatic and Chemical (DDEC6)[70–72] atomic population analysis. The idealized infinite 2D sheet of **Cu₂TTFtt** was used for simplicity, in lieu of the more complicated TMEDA capped structure. We also calculated a putative isolated 2D sheet of **Cu₂TTFtt**.

First, the magnetic ground states of **CuTTFtt**, **Cu₂TTFtt**, and isolated 2D sheets of **Cu₂TTFtt** were investigated, all of which converge to a closed-shell ground state with zero magnetization. In **Cu₂TTFtt**, the energy difference between the $S = 1$ and $S = 0$ states is significantly larger in the π-stacked system (0.337 eV) than in the isolated sheet (0.101 eV). This indicates that the π–π interactions in the stacked system make it increasingly favorable to pair electrons, promoting a closed-shell or antiferromagnetic coupling state. For **CuTTFtt**, the calculated energy gap between $S = 1$ and $S = 0$ is 0.203 eV, which is smaller than that of **Cu₂TTFtt**. In the $S = 1$ excited state, the majority of the spin density is localized on the TTFtt linkers, with 0.35 electrons residing on the in-chain Cu atom and no significant spin density on the out-of-chain Cu. This localization likely promotes convergence to a closed-shell solution. Comparison with the vacuum-isolated sheet shows that π-stacking interactions do not significantly change the spin delocalization in the $S = 1$ state.

The diamagnetism observed in **Cu₂TTFtt** aligns well with the calculated magnetic structure. The source of the paramagnetism observed in **CuTTFtt** is less clear. The smaller calculated energy gap between the closed-shell and $S = 1$ solutions suggests that a paramagnetic state is more reasonable in **CuTTFtt**. We also note the significantly lower high-temperature χT in **CuTTFtt** than would be expected for an $S = \frac{1}{2}$ paramagnet which is consistent with a comparatively large energy gap. However, it is difficult to rule out paramagnetic defect sites in this amorphous material. If some copper centers are structurally distorted they may behave as isolated paramagnets. In either case, computations support that paramagnetic behavior

is more reasonable in **CuTTFtt**, but deeper explorations of the magnetism of TTFtt CPs with paramagnetic metal centers are still warranted.

The band structure and DOS of **Cu₂TTFtt** were also analyzed to assess conductivity along different crystallographic directions (Fig. 6C). Along the Γ–Z and Y–T directions (the TTFtt polymer chain directions, Fig. 6A), a steep TTFtt-based band crossing the Fermi level indicates metallic conductivity mediated by TTFtt. Along Γ–Z, a flatter Cu-based band above the Fermi level suggests electron localization on Cu. Along Γ–Y (the Cu chain direction, orthogonal to the TTFtt chains), a Cu-based band crossing the Fermi level implies metallic conductivity mediated by Cu atoms.

Along Γ–X and S–Y (the π-stacking direction), two steep TTFtt-based bands crossing the Fermi level indicate high inter-stack conductivity, while a flatter Cu-based band just above the Fermi level in Γ–X suggests possible Cu electron localization. The DOS at the Fermi level is dominated by S p-orbitals, with notable contributions from C p- and Cu d-orbitals, highlighting the role of TTFtt π-electrons and Cu-mediated interactions in charge transport. To examine the role of π-stacking, we also analyzed isolated 2D sheets of **Cu₂TTFtt** (see SI Section 6). The band structure of the isolated sheets exhibits a 0.45 eV band gap located 0.3 eV above the Fermi level, with generally flatter bands. These findings confirm that π-stacking plays an important role in mediating conductivity along the polymer and Cu chains. However, we note the additional metallic directions between 1D chains in **Cu₂TTFtt**, which may lead to the higher conductivity in this material.

To test the effect of TMEDA, we calculated the DOS for the 2D **Cu₂TTFtt** system with TMEDA included (Fig. S28). The results confirm that TMEDA has negligible effect on the states near the Fermi level, supporting that its omission does not significantly affect the predicted electronic structure. Next, we consider the band structure and DOS of **CuTTFtt** to analyze the conductivity of the 1D chain along different crystallographic directions (Fig. 6D). The electronic band structure reveals multiple bands crossing the Fermi level, indicating metallic behavior. Along Γ–X (slightly off-axis to the π-stacking direction, Fig. 6B), two steep, TTFtt-based bands crossing the Fermi level suggest π-electron delocalization, while a flatter Cu-based band just above the Fermi level indicates electron localization on Cu. Along Γ–Z (the polymer chain direction), one Cu-based and one TTFtt-based band cross the Fermi level, indicating metallic character along the chain. Finally, along Γ–T (in-plane direction nearly perpendicular to the polymer chain), a less dispersive Cu-based band crossing the Fermi level suggests weaker interchain interactions. A 0.2 eV band gap appears at 1.4 eV above the Fermi level. The DOS at the Fermi level is primarily contributed by S p-orbitals, with notable C p- and Cu d-orbital contributions, again highlighting the influence of TTFtt π-electrons and Cu–TTFtt interactions in conductivity.

The band structure and DOS of **NiTTFtt** (Fig. S30A) are analyzed as a reference against **CuTTFtt** due to their different
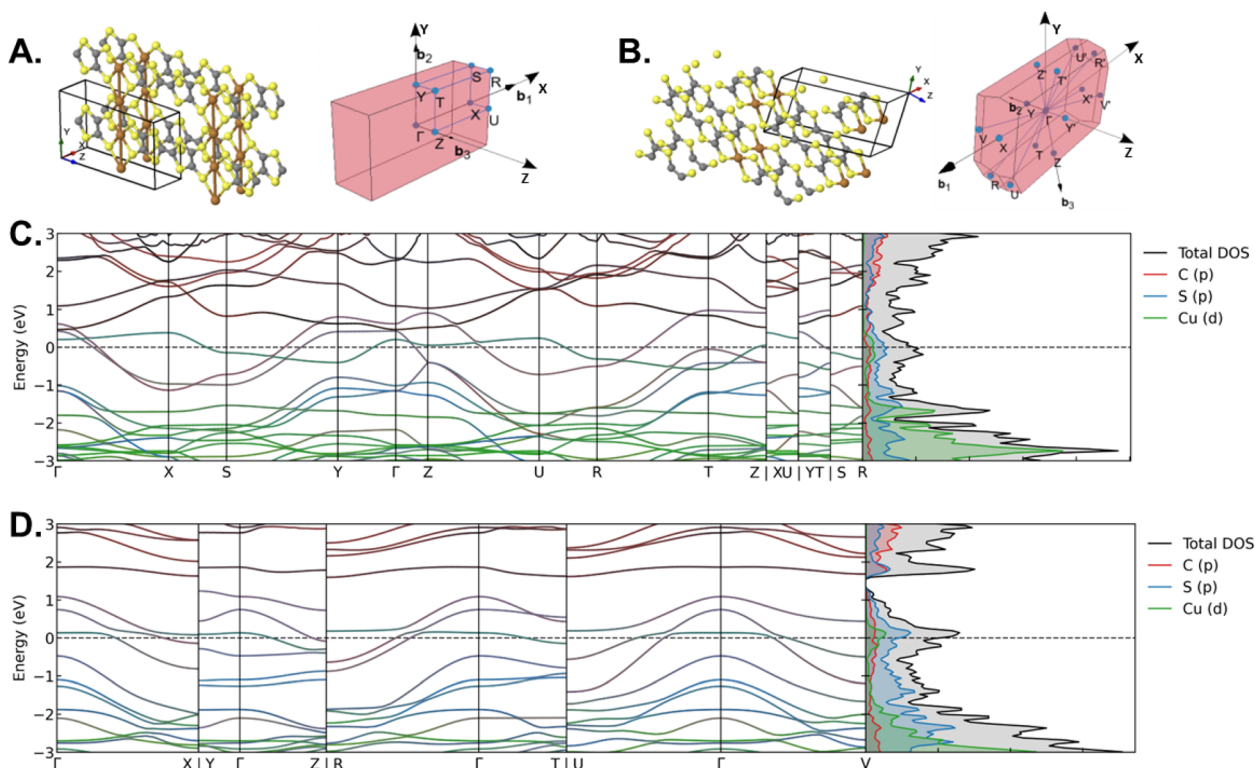

Fig. 6 Band structure and DOS for **Cu₂TTFtt** and **CuTTFtt**. (A) Primitive structure and Brillouin zone of the **Cu₂TTFtt** unit cell. (B) Primitive structure and Brillouin zone of the **CuTTFtt** unit cell. (C) Projected band structure and DOS for **Cu₂TTFtt** with the Fermi level denoted by black dashed lines. (D) Projected band structure and DOS for **CuTTFtt** with the Fermi level denoted by black dashed lines.

conductivities despite similar structural motifs and π-stacking interactions. Along the polymer chain and π-stacking directions, **NiTTFtt** exhibits metallic character, primarily driven by TTFtt with minimal Ni contributions. In contrast, a band gap appears along the in-plane direction nearly perpendicular to the polymer chain indicating hindered charge transport in this direction. **CuTTFtt** exhibits a higher DOS at the Fermi level, gradually decreasing to form a band gap, whereas **NiTTFtt** shows no such gap (Fig. S30B). Additionally, **CuTTFtt** shows more avoided crossings and flatter bands than **NiTTFtt**, suggesting more electron localization. The reduced band dispersion in **CuTTFtt** correlates with the experimentally observed higher conductivity in **NiTTFtt** relative to **CuTTFtt**.

Next, we compare the band structure and DOS of **Cu$_2$TTFtt** and **CuTTFtt** to examine how the additional orthogonal Cu chains in **Cu$_2$TTFtt** influence its metallic character. Along the polymer chain direction, **Cu$_2$TTFtt** has a more dispersive TTFtt-based band crossing the Fermi level compared to **CuTTFtt**. Additionally, in this direction, **Cu$_2$TTFtt** has a relatively flat Cu-based band above the Fermi level, while in **CuTTFtt**, the Cu-based band crosses the Fermi level. In **CuTTFtt**, along the in-plane direction nearly perpendicular to the polymer chain, a relatively flat Cu-based band again suggests some electron localization. In contrast, **Cu$_2$TTFtt** shows a highly dispersed band along the Cu chain direction, indicating strong metallic character. The 0.2 eV band gap observed at 1.4 eV above the Fermi level in **CuTTFtt** is absent in **Cu$_2$TTFtt**, as this gap is filled with a high density of bands from the additional Cu orbitals. Both materials display a similar total DOS at the Fermi level, but **CuTTFtt** shows a peak just above E_F that gradually decreases until forming the 0.2 eV gap (Fig. S30C).

Discussion

The generally steeper band crossing the Fermi level in **Cu$_2$TTFtt** compared to **CuTTFtt** strongly suggests higher electron mobility in **Cu$_2$TTFtt**. Combined with the smaller activation energy of **Cu$_2$TTFtt** relative to **CuTTFtt**, its electrical conductivity is expected to be higher, which is consistent with experiment. However, both compounds are theoretically predicted to be metallic, which contradicts the overall semiconducting behavior that is observed. We note that **NiTTFtt**, which is also predicted to be metallic, exhibits glassy metal behavior.[23] This discrepancy suggests that reduced crystallinity in all of these samples likely introduces localized states or increased electron scattering, significantly altering their electronic transport properties.

The significantly lower conductivity of **CuTTFtt** compared to **NiTTFtt** is noteworthy. In several conductive reticular materials, Cu-based compounds typically exhibit higher conductivity than their Ni analogs with the same ligands, such as benzene-hexathiolate and hexaiminobenzene.[2] This divergent behavior in TTFtt^{2-}-based materials may be attributed to the triplet diradical nature of TTFtt^{2-} (ref. 73) and suggests that magnetic metal centers, such as Cu^{2+}, are detrimental to electrical conductivity when putatively magnetic linkers are present. This may plausibly arise from some degree of coupling between the paramagnetic centers and the TTFtt-based electrons which serve as carriers.

Although theoretical calculations suggest that the 2D structure of **Cu$_2$TTFtt** should result in electronic conductivity comparable to that of amorphous **NiTTFtt**, experimental results reveal that the conductivity of **Cu$_2$TTFtt** is actually one order of magnitude lower. This counterintuitive result can be primarily attributed to the presence of TMEDA, which coordinates with Cu^{2+} centers and acts as an insulating barrier at the grain boundaries, thereby impeding efficient charge transport between crystallites. In contrast, **NiTTFtt** contains no organic components beyond TTFtt itself, allowing for strong π–π interactions between chains that promote effective interchain electron transfer. Possible strategies to further enhance the conductivity of **Cu$_2$TTFtt** include substituting TMEDA with smaller amines, performing post-synthetic ligand exchange, and optimizing growth/annealing conditions to enlarge crystallite sizes.

Multiple independent measurements indicate that **Cu$_2$TTFtt** is mixed-valent, with coexisting Cu$^+$ and Cu^{2+} centers. Mixed valency has been reported more frequently in iron-based conductive coordination polymers, where Fe^{2+}/Fe^{3+} delocalization can enhance charge transport.[74] By analogy, similar mechanisms may facilitate conductivity in **Cu$_2$TTFtt** even though the macroscopic conductivity is likely limited by grain-boundary effects. The presence of Cu$^+$ may also be structurally consequential: it likely contributes to stabilizing the 2D ribbon-like architecture observed for **Cu$_2$TTFtt**. In particular, prior studies on poly[Cu$_x$(Cu-ETT)] plausibly feature related structural/valence motifs,[36] whereas analogous 2D arrangements have not been reported for Ni-based TTFtt or ETT systems—as expected due to the much lower stability of Ni$^+$ relative to Cu$^+$. Collectively, these considerations highlight the importance of Cu$^+$ in stabilizing 2D networks and suggest that mixed valency may serve as an additional feature for tuning structure and charge transport in TTFtt-based coordination polymers.

Cu$_2$TTFtt, with its 2D structure and strong antiferromagnetic (AFM) interactions, bears some similarity to the layered cuprate materials, which exhibit high-temperature superconductivity.[75] In cuprates, doping introduces charge carriers that suppress long-range AFM ordering and enable unconventional superconducting states. We speculate that a similar approach in **Cu$_2$TTFtt**, specifically doping at the Cu sites or modulating the redox state of the TTFtt ligand, may result in interesting electronic and magnetic properties. This is particularly compelling given the interplay of 2D geometry, AFM interactions, and the potential for doping-induced charge delocalization in **Cu$_2$TTFtt**. Experimental exploration of doping strategies and their effects on the electronic density of states, along with theoretical studies to identify accessible pairing mechanisms, are exciting future areas of study.

Conclusions

In this study, two new copper-TTFtt-based coordination polymers, **CuTTFtt** and **Cu$_2$TTFtt** have been successfully synthesized

and characterized. The isolation of these materials was made possible by leveraging pre-synthetic redox control of the TTFtt ligand, where differentially oxidized transmetalation precursors provide access to the two different materials. Structural analyses using PXRD, PDF and EXAFS methods reveal that **CuTTFtt** adopts an amorphous 1D chain structure, while **Cu₂TTFtt** features a 2D ribbon-like layered framework due to the inclusion of ribbon-capping TMEDA molecules.

Comprehensive spectroscopic studies, including sulfur and copper K-edge XAS, Raman spectroscopy, and XPS, demonstrate that the oxidation states of the TTFtt ligand and Cu centers play a critical role in determining the electronic and magnetic properties of these materials. The material **CuTTFtt** features an oxidized $TTFtt^{2-}$ state, while the spectroscopic evidence supports a reduced formally $(Cu^{2+})(Cu^{+})(TTFtt^{3-})$ electronic structure in **Cu₂TTFtt**. These results further underscore the importance of precise redox state determination in sulfur-based coordination systems.

Electrical conductivity measurements show that both materials are highly conductive, with room-temperature values of $23(2)$ S cm^{-1} for **CuTTFtt** and $50(2)$ S cm^{-1} for **Cu₂TTFtt**. The higher conductivity of **Cu₂TTFtt** is due to some combination of higher carrier densities or enhanced charge mobility as based on DFT calculations. Magnetic studies reveal contrasting behaviors. 1D **CuTTFtt** displays paramagnetic behavior, while **Cu₂TTFtt** is diamagnetic, likely due to strong antiferromagnetic coupling interactions. These observations provide insight into the interplay between magnetic properties, dimensionality, and electronic properties in CPs containing redox-active ligands.

In conclusion, this work demonstrates the importance of redox state control and dimensionality in tuning the structural, electronic, and magnetic properties of TTFtt-based CPs, particularly as paramagnetic ions are included into these materials. The different structures arising from differentially oxidized precursors represents a new pathway for controlling material dimensionality and crystallinity. The inclusion of TMEDA in **Cu₂TTFtt** also raises the possibility of modulating TTFtt-based materials with additional organic components. By bridging theoretical predictions and experimental realization, this study provides important insights into the rational design of highly conductive and magnetically tunable coordination materials.

Author contributions

N. J. and J. S. A. conceived and designed the study. N. J. performed the majority of the experimental work. S. V. and J.-N. B. carried out the theoretical calculations. C.-Y. L. conducted variable-temperature electrical resistance measurements and scanning electron microscopy analyses. H. L. N. built the structural model. J. H. and K. W. C. performed structural characterization and analysis. J.-H. C. and S. P. conducted electrical conductivity and Seebeck coefficient measurements. A. R. and H. S. L. performed UV-vis and X-ray absorption spectroscopy measurements and subsequent data analysis. A. S. F. conducted X-ray photoelectron spectroscopy studies and

contributed to structural analysis. All authors participated in writing and revising the manuscript.

Conflicts of interest

There are no conflicts to declare.

Data availability

Data for this article, including experimental details, composition characterizations, structural characterizations, spectroscopic characterizations, physical property measurements, and theoretical calculation details are available in SI. Supplementary information is available. See DOI: https://doi.org/10.1039/d5sc03070f.

Acknowledgements

References

1 G. Givaja, P. Amo-Ochoa, C. J. Gómez-García and F. Zamora, *Chem. Soc. Rev.*, 2012, **41**, 115–147.

2 L. S. Xie, G. Skorupskii and M. Dinca, *Chem. Rev.*, 2020, **120**, 8536–8580.

3 M. Wang, R. Dong and X. Feng, *Chem. Soc. Rev.*, 2021, **50**, 2764–2793.

4 Z. Meng and K. A. Mirica, *Nano Res.*, 2021, **14**, 369–375.

5 A. Aykanat, Z. Meng, R. M. Stolz, C. T. Morrell and K. A. Mirica, *Angew. Chem.*, 2022, **134**, e202113665.

6 H. Roh, T. J. Quill, G. Chen, H. Gong, Y. Cho, H. J. Kulik, Z. Bao, A. Salleo and A. Gumyusenge, *ACS Nano*, 2025, **19**, 6332–6341.

7 M.-S. Yao, K.-I. Otake and S. Kitagawa, *Trends Chem.*, 2023, **5**, 588–604.

8 H. Maeda, K. Takada, N. Fukui, S. Nagashima and H. Nishihara, *Coord. Chem. Rev.*, 2022, **470**, 214693.

9 Y. Lu, P. Samorì and X. Feng, *Acc. Chem. Res.*, 2024, **57**, 1985–1996.

10 D. Feng, T. Lei, M. R. Lukatskaya, J. Park, Z. Huang, M. Lee, L. Shaw, S. Chen, A. A. Yakovenko, A. Kulkarni, J. Xiao, K. Fredrickson, J. B. Tok, X. Zou, Y. Cui and Z. Bao, *Nat. Energy*, 2018, **3**, 30–36.

11 M. L. Aubrey, B. M. Wiers, S. C. Andrews, T. Sakurai, S. E. Reyes-Lillo, S. M. Hamed, C.-J. Yu, L. E. Darago, J. A. Mason, J.-O. Baeg, F. Grandjean, G. J. Long, S. Seki, J. B. Neaton, P. Yang and J. R. Long, *Nat. Mater.*, 2018, **17**, 625–632.

12 P. H. Le, L. B. Zasada and D. J. Xiao, *Acc. Chem. Res.*, 2025, **58**, 1776–1785.

13 J. Xie, L. Wang and J. S. Anderson, *Chem. Sci.*, 2020, **11**, 8350–8372.

14 Y. Kamakura and D. Tanaka, *Chem. Lett.*, 2021, **50**, 523–533.

15 A. J. Clough, J. W. Yoo, M. H. Mecklenburg and S. C. Marinescu, *J. Am. Chem. Soc.*, 2015, **137**, 118–121.

16 C. A. Downes and S. C. Marinescu, *J. Am. Chem. Soc.*, 2015, **137**, 13740–13743.

17 X. Huang, H. Li, Z. Tu, L. Liu, X. Wu, J. Chen, Y. Liang, Y. Zou, Y. Yi, J. Sun, W. Xu and D. Zhu, *J. Am. Chem. Soc.*, 2018, **140**, 15153–15156.

18 R. Dong, P. Han, H. Arora, M. Ballabio, M. Karakus, Z. Zhang, C. Shekhar, P. Adler, P. S. Petkov, A. Erbe, S. C. B. Mannsfeld, C. Felser, T. Heine, M. Bonn, X. Feng and E. Cánovas, *Nat. Mater.*, 2018, **17**, 1027–1032.

19 C. Lu, J. Y. Choi, B. Check, X. Fang, S. Spotts, D. Nuñez and J. Park, *J. Am. Chem. Soc.*, 2024, **146**, 26313–26319.

20 L. Wang and J. S. Anderson, *Chem. Mater.*, 2024, **36**, 3999–4010.

21 L. Wang, A. Sarkar, G. L. Grocke, D. W. Laorenza, B. Cheng, A. Ritchhart, A. S. Filatov, S. N. Patel, L. Gagliardi and J. S. Anderson, *J. Am. Chem. Soc.*, 2023, **145**, 8486–8497.

22 J. Xie, J.-N. Boyn, A. S. Filatov, A. J. McNeece, D. A. Mazziotti and J. S. Anderson, *Chem. Sci.*, 2020, **11**, 1066–1078.

23 J. Xie, S. Ewing, J.-N. Boyn, A. S. Filatov, B. Cheng, T. Ma, G. L. Grocke, N. Zhao, R. Itani, X. Sun, H. Cho, Z. Chen, K. W. Chapman, S. N. Patel, D. V. Talapin, J. Park, D. A. Mazziotti and J. S. Anderson, *Nature*, 2022, **611**, 479–484.

24 R. P. Shibaeva and E. B. Yagubskii, *Chem. Rev.*, 2004, **104**, 5347–5378.

25 A. Kobayashi, E. Fujiwara and H. Kobayashi, *Chem. Rev.*, 2004, **104**, 5243–5264.

26 H. Poleschner, W. John, G. Kempe, E. Hoyer and E. Fanghänel, *Z. Chem.*, 1978, **18**, 345–346.

27 N. M. Rivera, E. M. Engler and R. R. Schumaker, *J. Chem. Soc., Chem. Commun.*, 1979, 184–185.

28 N. Yoshioka, H. Nishide, K. Inagaki, K. Inagaki and E. Tsuchida, *Polym. Bull.*, 1990, **23**, 631–636.

29 Y. Tang, X. Gan, M. Tan and X. Zheng, *Synth. Met.*, 1998, **97**, 43–46.

30 S. Dahm, W. Strunz, H. J. Keller and D. Schweitzer, *Synth. Met.*, 1993, **55**, 884–889.

31 K. Ueda, R. Fukuzaki, T. Ito, N. Toyama, M. Muraoka, T. Terao, K. Manabe, T. Hirai, C.-J. Wu and S.-C. Chuang, *J. Am. Chem. Soc.*, 2022, **144**, 18744–18749.

32 J. R. Reynolds, J. C. Chien and C. P. Lillya, *Macromolecular*, 1987, **20**, 1184–1191.

33 C. Dirk, M. Bousseau, P. Barrett, F. Moraes, F. Wudl and A. Heeger, *Macromolecular*, 1986, **19**, 266–269.

34 Z. Liu, T. Liu, C. N. Savory, J. P. Jurado, J. S. Reparaz, J. Li, L. Pan, C. F. Faul, I. P. Parkin and G. Sankar, *Adv. Funct. Mater.*, 2020, **30**, 2003106.

35 S. Alvarez, R. Vicente and R. Hoffmann, *J. Am. Chem. Soc.*, 1985, **107**, 6253–6277.

36 P. Sheng, Y. Sun, F. Jiao, C. Liu, W. Xu and D. Zhu, *Synth. Met.*, 2014, **188**, 111–115.

37 T. Chen, J.-H. Dou, L. Yang, C. Sun, J. J. Oppenheim, J. Li and M. Dincă, *J. Am. Chem. Soc.*, 2022, **144**, 5583–5593.

38 H. Furukawa, J. Kim, N. W. Ockwig, M. O'Keeffe and O. M. Yaghi, *J. Am. Chem. Soc.*, 2008, **130**, 11650–11661.

39 J. Xiao, J. Han, C. Zhang, G. Ling, F. Kang and Q. H. Yang, *Adv. Energy Mater.*, 2022, **12**, 2100775.

40 J. Xie, J.-A. Pan, B. Cheng, T. Ma, A. S. Filatov, S. N. Patel, J. Park, D. V. Talapin and J. S. Anderson, *J. Am. Chem. Soc.*, 2022, **144**, 19026–19037.

41 T. Chen, J.-H. Dou, L. Yang, C. Sun, N. J. Libretto, G. Skorupskii, J. T. Miller and M. Dincă, *J. Am. Chem. Soc.*, 2020, **142**, 12367–12373.

42 D. Sheberla, J. C. Bachman, J. S. Elias, C.-J. Sun, Y. Shao-Horn and M. Dincă, *Nat. Mater.*, 2017, **16**, 220–224.

43 Y. Jiang, I. Oh, S. H. Joo, Y.-S. Seo, S. H. Lee, W. K. Seong, Y. J. Kim, J. Hwang, S. K. Kwak and J.-W. Yoo, *J. Am. Chem. Soc.*, 2020, **142**, 18346–18354.

44 X. Huang, S. Zhang, L. Liu, L. Yu, G. Chen, W. Xu and D. Zhu, *Angew. Chem.*, 2018, **130**, 152–156.

45 X. Huang, P. Sheng, Z. Tu, F. Zhang, J. Wang, H. Geng, Y. Zou, C.-a. Di, Y. Yi and Y. Sun, *Nat. Commun.*, 2015, **6**, 7408.

46 P. M. Crossland, C.-Y. Lien, L. O. de Jong, J. L. Spellberg, M. E. Czaikowski, L. Wang, A. S. Filatov, S. B. King and J. S. Anderson, *J. Am. Chem. Soc.*, 2024, **146**, 33608–33615.

47 L. Mendecki, M. Ko, X. Zhang, Z. Meng and K. A. Mirica, *J. Am. Chem. Soc.*, 2017, **139**, 17229–17232.

48 X. Huang, Y. Qiu, Y. Wang, L. Liu, X. Wu, Y. Liang, Y. Cui, Y. Sun, Y. Zou and J. Zhu, *Angew. Chem.*, 2020, **132**, 22791–22798.

49 Y. Kobayashi, T. Terauchi, S. Sumi and Y. Matsushita, *Nat. Mater.*, 2017, **16**, 109–114.

50 J. T. York, E. C. Brown and W. B. Tolman, *Angew. Chem., Int. Ed.*, 2005, **44**, 7745–7748.

51 A. Neuba, R. Haase, W. Meyer-Klaucke, U. Flörke and G. Henkel, *Angew. Chem., Int. Ed.*, 2012, **51**, 1714–1718.

52 J. Folmer and F. Jellinek, *J. Less-Common Met.*, 1980, **76**, 153–162.

53 P. Kumar, R. Nagarajan and R. Sarangi, *J. Mater. Chem. C*, 2013, **1**, 2448–2454.

54 N. Jiang, J.-N. Boyn, A. Ramanathan, H. S. La Pierre and J. S. Anderson, *Chem. Commun.*, 2023, **59**, 9537–9540.

55 T. Petrenko, K. Ray, K. E. Wieghardt and F. Neese, *J. Am. Chem. Soc.*, 2006, **128**, 4422–4436.

56 S. Mugiraneza and A. M. Hallas, *Commun. Phys.*, 2022, **5**, 95.

57 S. Stoll and A. Schweiger, *J. Magn. Reson.*, 2006, **178**, 42–55.

58 R. Kirmse, S. Saluschke, S. Ritter and W. Dietzsch, *Z. Anorg. Allg. Chem.*, 1993, **619**, 576–582.

59 G. Kresse and J. Hafner, *Phys. Rev. B: Condens. Matter Mater. Phys.*, 1993, **47**, 558.

60 G. Kresse and J. Furthmüller, *Comput. Mater. Sci.*, 1996, **6**, 15–50.

61 G. Kresse and J. Furthmüller, *Phys. Rev. B: Condens. Matter Mater. Phys.*, 1996, **54**, 11169.

62 J. P. Perdew, K. Burke and M. Ernzerhof, *Phys. Rev. Lett.*, 1996, **77**, 3865.

63 G. Kresse and J. Hafner, *J. Condens Matter. Phys.*, 1994, **6**, 8245.

64 G. Kresse and D. Joubert, *Phys. Rev. B: Condens. Matter Mater. Phys.*, 1999, **59**, 1758.

65 Y. Hinuma, G. Pizzi, Y. Kumagai, F. Oba and I. Tanaka, *Comput. Mater. Sci.*, 2017, **128**, 140–184.

66 A. Togo, K. Shinohara and I. Tanaka, *Sci. Technol. Adv. Mater.: Methods*, 2024, **4**, 2384822.

67 A. H. Larsen, J. J. Mortensen, J. Blomqvist, I. E. Castelli, R. Christensen, M. Dułak, J. Friis, M. N. Groves, B. Hammer and C. Hargus, *J. Condens Matter. Phys.*, 2017, **29**, 273002.

68 S. Grimme, S. Ehrlich and L. Goerigk, *J. Comput. Chem.*, 2011, **32**, 1456–1465.

69 A. M. Ganose, A. J. Jackson and D. O. Scanlon, *J. Open Source Softw.*, 2018, **3**, 717.

70 T. A. Manz and N. G. Limas, *RSC Adv.*, 2016, **6**, 47771–47801.

71 N. G. Limas and T. A. Manz, *RSC Adv.*, 2016, **6**, 45727–45747.

72 T. A. Manz, *RSC Adv.*, 2017, **7**, 45552–45581.

73 A. Kawamura, J. Xie, J.-N. Boyn, K. A. Jesse, A. J. McNeece, E. A. Hill, K. A. Collins, J. A. Valdez-Moreira, A. S. Filatov, J. W. Kurutz, D. A. Mazziotti and J. S. Anderson, *J. Am. Chem. Soc.*, 2020, **142**, 17670–17680.

74 L. S. Xie, L. Sun, R. Wan, S. S. Park, J. A. DeGayner, C. H. Hendon and M. Dincă, *J. Am. Chem. Soc.*, 2018, **140**, 7411–7414.

75 N. Plakida, *High-temperature cuprate superconductors: Experiment, theory, and applications*, Springer Science & Business Media, 2010.